Characterizing coherent structures in Bose-Einstein condensates through dynamic-mode decomposition

Christopher W. Curtis,[1,2] R. Carretero-González,[1,2] and Matteo Polimeno[1]

[1]*Nonlinear Dynamical Systems Group, Department of Mathematics and Statistics, San Diego State University, San Diego, California 92182-7720, USA*

[2]*Computational Sciences Research Center, San Diego State University, San Diego, California 92182-7720, USA*

(Received 29 January 2019; published 19 June 2019)

We use the dynamic mode decomposition (DMD) methodology to study weakly turbulent flows in two-dimensional Bose-Einstein condensates modeled by a Gross-Pitaevskii equation subject to band-limited stochastic forcing. The forcing is balanced by the removal of energy at both ends of the energy spectrum through phenomenological hypoviscosity and hyperviscosity terms. Using different combinations of these parameters, we simulate three different regimes corresponding to weak-wave turbulence, and high- and low-frequency saturation. By extracting and ranking the primary DMD modes carrying the bulk of the energy, we are able to characterize the different regimes. In particular, the proposed DMD mode projection is able to seamlessly extract the vortices present in the condensate. This is achieved despite the fact that we do not use any phase information of the condensate as it is usually not directly available in realistic atomic BEC scenarios. Being model independent, this DMD methodology should be portable to other models and experiments involving complex flows. The DMD implementation could be used to elucidate different types of turbulent regimes as well as identifying and pinpointing the existence of delicate and hidden coherent structures within complex flows.

DOI: 10.1103/PhysRevE.99.062215

I. INTRODUCTION

Building on existing experiments [1–6] and the recent observation of turbulent cascades in a Bose-Einstein condensate (BEC) [7], it is important to better understand and characterize, in as quantitative a means as possible, the complex dynamics associated with turbulence in dispersive, nonlinear-wave systems. While small-amplitude states whose statistics remain nearly Gaussian permit a relatively complete analytic characterization of turbulent cascades—embodied in the weak-wave turbulence (WWT) theory initiated in Ref. [8] and collected in Ref. [9] as noted in Refs. [10,11]—the assumptions which one makes to derive results in WWT necessarily must generically break down over long-enough time scales.

This breakdown is best characterized by the formation of long-wavelength, larger-amplitude coherent structures (CSs). In classic, one-dimensional systems, characterizing such structures in terms of solitons is relatively straightforward; see, for example, Ref. [11]. However, in two dimensions (2D), and for systems like the Gross-Pitaevskii equation (GPE) or defocusing nonlinear Schrödinger equation (NLSE), describing coherent structures in quantitative terms is far more challenging. In the context of BECs, existing methodologies for characterizing CSs are based on heuristic statistical metrics [12]. In the broader context of two-dimensional WWT, along with classic approaches built around studying qualitative features in Fourier transforms, methods based on tracking spikes in Gaussian curvature of the solution were described in Ref. [13]. However, CSs in BECs are not readily characterized as high curvature structures. Instead, the formation of CSs corresponds to the elimination of vortices and the emission of sound waves on the rising-amplitude-background-condensed state [12]. Thus long-time, highly evolved BEC flows can be composed of relatively few vortices hidden behind a wide range of propagating acoustic waves. Moreover, vortices have been shown to play an important role is the manifestation of BEC turbulence [2,14,15]. However, identification of vortices is particularly problematic in standard, atomic, BEC experiments where only the density is readily accessible [16–19]. Easily identifiable features of the flow are then both scarce and difficult to reliably identify, making characterization of the transition away from the WWT state difficult. In this paper, to address this shortcoming, we study the use of the dynamic-mode decomposition (DMD) [20–23], which is a modal decomposition generated by discrete snapshots of the spatiotemporal evolution of the system under consideration. The advantage of the DMD is in its great flexibility due to it being a model-free means of analyzing flows.

By developing an adaptive mode selection strategy, we are able to algorithmically decompose 2D BEC flows into a mean and a series of ranked fluctuations. This is done for purely WWT flows in which long-wavelength damping suppresses the appearance of CSs and for flows in which energy is allowed to accumulate at long wavelengths, thereby allowing the nucleation of CSs. As we see from numerical simulations, the temporal mean of the DMD dynamics provides a relatively smooth, in effect denoised, visualization of CSs. This allows for the ready visualization of those few vortices which remain after the long-time transition from the low-amplitude four-wave mixing state to a nearly constant background, three-wave mixing state mediated by sound waves traveling along

the background; see Refs. [9,12,24] for more details on these transitions and states.

Our adaptive mode identification scheme extracts and ranks the number of modes needed to represent 90% of the relative energy of the flow. For all the flows studied, over longer time scales, at most on the order of 10% of the total number of modes is needed to meet this selection threshold. Thus we show for these BEC complex flows that relatively small subspaces can be used to accurately describe the dynamics. Moreover, we see that the complexity of a flow is well encoded by the size of the subspace needed to capture the 90% relative-energy threshold, with fully turbulent flows devoid of CSs requiring the greatest number of modes and flows allowing for long-wavelength CSs requiring the least. Therefore, the DMD may also provide a quantitative means of identifying the degree of complexity in flows and thus puts forward an interesting future avenue for identifying novel and useful statistical quantities facilitating flow classification. While we have performed this study in the context of BECs, our approach to identifying the most significant DMD modes should prove useful in other contexts where complex flows prevent ready classification of significant features.

The structure of the paper is as follows. In Sec. II we introduce the BEC model that will be the subject of our study and some generic aspect of WWT. Section III is devoted to describe the DMD methodology. In Sec. IV we apply this DMD methodology to characterize BEC flows in different regimes, namely, the WWT, the low-frequency saturation, and the high-frequency saturation regimes. Finally, in Sec. V we summarize our results and bring forward a few interesting avenues for further investigation.

II. MODELING AND WEAK-WAVE TURBULENCE

In nondimensional coordinates (see Appendix A for details on the 3D to 2D reduction and the nondimensionalization), we model the BEC through a stochastically forced GPE [9,12]

$$i\psi_t = -\Delta\psi + |\psi|^2\psi + \gamma_f - i(\nu_h\Delta^p + \nu_l\tilde{\Delta}^{-p})\psi. \tag{1}$$

The GPE without the phenomenologically added damping and forcing terms is known to be a rigorous accurate approximation to the behavior of large ensembles of low-temperature bosons [25]. Our choice of forcing and damping are made in order to explore more complex dynamics of the GPE. Here $\psi(\mathbf{x},t)$ is the wave function in 2D space [$\mathbf{x}=(x,y)$], which we restrict to satisfying periodic-boundary conditions in both directions with common period $2L$. Thus we have the equivalent Fourier representation for ψ:

$$\psi(\mathbf{x},t) = \sum_{\mathbf{m}} a_{\mathbf{m}}(t)e^{i\mathbf{k}_{\mathbf{m}}\cdot\mathbf{x}}, \tag{2}$$

$$[1.0ex]\mathbf{m} = (m,n), \quad \mathbf{k}_{\mathbf{m}} = \frac{\pi}{L}\mathbf{m}. \tag{3}$$

Likewise, Δ denotes the 2D Laplacian, $\gamma_f(\mathbf{x},t)$ is the stochastic forcing (see below), and the terms with coefficients ν_h and ν_l correspond to hyperviscosity and hypoviscosity introduced with the high-order Laplacian Δ^p. The regularized Laplacian $\tilde{\Delta}$ is defined through the Fourier transform of its symbol:

$$\widehat{\tilde{\Delta}} = -\begin{cases} |\mathbf{k}_{\mathbf{m}}|^2, & \mathbf{m}\neq 0, \\ \left(\frac{\pi}{L}\right)^2, & \mathbf{m}=0. \end{cases} \tag{4}$$

We thus set the zero mode to one to avoid spurious divergences when numerically integrating the system. Note that we always remain in the defocusing, or "dark," case [26] and that we initialize our system with zero initial conditions, i.e., $\psi(\mathbf{x},t=0)=0$. The forcing γ_f is chosen so as to be the spectrally band limited function

$$\gamma_f(\mathbf{x},t) = \gamma_0\, e^{2\pi i\varphi(t)} \sum_{k_l\leqslant||\mathbf{k}_{\mathbf{m}}||_2\leqslant k_h} e^{i\mathbf{k}_{\mathbf{m}}\cdot\mathbf{x}}, \tag{5}$$

where $||\mathbf{k}_{\mathbf{m}}||_2 = \frac{\pi}{L}\sqrt{m^2+n^2}$, γ_0 is the strength of the forcing, and the phase $\varphi(t)$ is chosen as a random variable uniformly distributed between zero and 1. Thus our forcing is characterized by an injection range of wave numbers via the choices of a "low" wave number threshold k_l and a "high" wave number threshold k_h. We likewise see that the forcing is unbiased in any particular spatial direction so that, by starting with zero-initial conditions, the solution $\psi(\mathbf{x},t)$ largely mimics the forcing until it has reached a large enough amplitude that nonlinearity, through four-wave mixing, is able to transfer energy across Fourier modes. The injection of energy through the forcing $\gamma_f(\mathbf{x},t)$ is ultimately balanced against the strength of the hyperviscosity characterized by the magnitude of ν_h and the hypoviscosity characterized by the magnitude of ν_l.

We take the period $2L \gg 1$ so as to allow for long-wavelength phenomena and space for large numbers of vortices to form and interact. We note that the question of what constitutes a "large" domain is somewhat ambiguous in this problem due to the forcing. Typically, when modeling a BEC, a length scale is set via the "healing length" [24], which ultimately determines the width of vortices in the GPE. However, to do this one must have a fixed particle number $\mathcal{N} = \int|\psi|^2 d\mathbf{x}$, but due to the forcing and viscosity we have that

$$\frac{1}{2}\frac{d\mathcal{N}}{dt} = \mathrm{Im}\left\{\int \gamma_f(\mathbf{x},t)\psi^* d\mathbf{x}\right\} - \int \psi^*(\nu_h\Delta^p + \nu_l\tilde{\Delta}^{-p})\psi\, d\mathbf{x}, \tag{6}$$

so that the particle number, and thus the chosen length scale, necessarily change with time. Ultimately though, for long times, a quasiequilibrium is achieved through the balance of injection due to the forcing γ_f and the particle removal or energy dissipation due to the hyperviscosity removing high-frequency modes and the hypoviscosity removing low-frequency modes.

By stochastically forcing the system starting from a zero-amplitude configuration, we are able to generate a WWT state at some point in the temporal evolution of the flow. This is characterized as complex flows driven by nontrivial fluxes of energy and particle count across ranges of wave numbers. To quantify this concept with respect to the energy, we define the associated isotropic energy density $E_d(k,t)$ as

$$E_d(k,t) = 2\pi k\,\omega(k)\,n(k,t), \tag{7}$$

where $\omega(k)$ is the dispersion relationship of the GPE, and $n(k,t)$ is given by

$$n(k,t) = \langle |a_{\mathbf{m}}(t)|^2 \rangle, \quad ||\mathbf{m}||_2 = k, \tag{8}$$

where $\langle\cdot\rangle$ denotes averaging over modes with constant wave number k. Associated with the energy density is an affiliated energy flux ϵ so that

$$\partial_t E_d + \partial_k \epsilon \sim 0. \tag{9}$$

It is one of the major achievements in the WWT theory that one can derive Boltzmann-like kinetic equations describing the evolution of $n(k,t)$ [9]. Thus, by looking for flows in which the energy density is in quasiequilibrium so that $\partial_t E_d \sim 0$, which therefore implies that $\partial_t n(k,t) \sim 0$, we can then distinguish quasiequilibrium profiles of $E_d(k,t)$ by whether $\epsilon \sim 0$ or $\epsilon \sim c$, where c is some constant. The zero case corresponds to no energy flux, thereby describing a thermodynamically steady state associated with the equipartition of energy. It is the nonzero energy flux states which distinguish WWT states, and those that we are most interested in studying. As noted in Ref. [9], the cascade associated with energy is from long to short length scales, or from small to large values of k. In contrast, while there is a cascade attributable to the other naturally conserved quantity of the GPE, i.e., the total particle count, the cascade in that case is described as "warm," meaning that it is made up of nontrivial and trivial flux contributions; see Ref. [9] for further details.

III. DYNAMIC-MODE DECOMPOSITION

For completeness, we review some details of the DMD methodology. In what follows, we choose the measurable quantity $g^{(l)}(t) = |\psi(\mathbf{x}_l, t)|$ or

$$g^{(l)}(t) = \left| \sum_{0 \leqslant ||\mathbf{m}||_\infty \leqslant K} a_{\mathbf{m}}(t) e^{i\mathbf{k}_{\mathbf{m}} \cdot \mathbf{x}_l} \right|, \tag{10}$$

where we sample at the $l = 1, \ldots, (2K+1)^2$ points $\mathbf{x}_l$ in the affiliated numerical mesh. This choice corresponds to sampling the *magnitude* of the wave function ψ at the mesh points of our numerical simulations. In typical BEC experiments, the direct observable is the density that is proportional to $|\Psi|^2$ and thus the magnitude $|\Psi|$ is readily available (using $|\Psi|^2$ instead of $|\Psi|$ does not alter the results presented herein). The DMD method in the context of this paper consists of first generating a sequence of $N+1$ samples of $g^{(l)}$, say $g_n^{(l)} = g^{(l)}(t_n)$, at times $t_n = n\delta t$, $n = 0, \ldots, N$. Connecting the two time states corresponds to a linear operator, called the Koopman Operator [23], which we denote by $e^{\mathcal{L}\delta t}$, so that

$$\mathbf{g}_{n+1} = e^{\mathcal{L}\delta t} \mathbf{g}_n, \quad \mathbf{g}_n = \left\{ g_n^{(l)} \right\}_{l=1}^{(2K+1)^2}, \tag{11}$$

where the superscripts are used to denote space while the subscripts denote time. In Appendix B, we explain some of the original physical motivation introduced in Ref. [27], used elsewhere for data reduction and analysis in Ref. [28], to help provide insight as to why the DMD method is effective.

Defining the $(2K+1)^2 \times N$ matrices V_1 and V_2, where

$$V_1 = \left\{ \begin{pmatrix} g_0^{(1)} \\ \vdots \\ g_0^{(2K+1)^2} \end{pmatrix} \cdots \begin{pmatrix} g_{N-1}^{(1)} \\ \vdots \\ g_{N-1}^{(2K+1)^2} \end{pmatrix} \right\},$$

$$V_2 = \left\{ \begin{pmatrix} g_1^{(1)} \\ \vdots \\ g_1^{(2K+1)^2} \end{pmatrix} \cdots \begin{pmatrix} g_N^{(1)} \\ \vdots \\ g_N^{(2K+1)^2} \end{pmatrix} \right\}, \tag{12}$$

the DMD approximates $e^{\mathcal{L}\delta t}$ (see Appendix B) via a finite-dimensional matrix A given by

$$S = U^\dagger A U = U^\dagger V_2 W \Sigma^{-1}, \tag{13}$$

where we have used a singular value decomposition (SVD) of V_1 so that $V_1 = U\Sigma W^\dagger$, where U and W are matrices of sizes $(2K+1)^2 \times N$ and $N \times N$, respectively, whose columns form orthonormal sets of vectors, and Σ is an $N \times N$ diagonal matrix containing the singular values of V_1, which are the non-negative square roots of the non-negative eigenvalues of $V_1^\dagger V_1$. This in effect makes A the least-squares solution to the nonsquare matrix problem

$$V_2 = A V_1, \tag{14}$$

corresponding to the one-step time map between V_1 and V_2. Therefore, by computing the associated eigenvalues and eigenvectors of S, say μ_j and $\tilde{\phi}_j$, respectively, then, for N large enough with sufficiently controlled spacing in the time series, these eigenvalues and eigenvectors will approximate those of $e^{\mathcal{L}\delta t}$. Likewise, this allows us to write each vector $\mathbf{g}_n$ in our time series as

$$\mathbf{g}_n = \sum_{j=1}^{N} b_j \mu_j^n \phi_j + \mathbf{r}_n, \quad \phi_j = U\tilde{\phi}_j, \tag{15}$$

where $\mathbf{r}_n$ denotes the residual at the nth sampling time and the coefficients b_j are found from the initial condition

$$\mathbf{g}_0 = \sum_{j=1}^{N} b_j \phi_j. \tag{16}$$

See Ref. [29] for a recent exposition which studies the convergence of DMD generated spectral information to the spectral information of the affiliated Koopman operator.

IV. CHARACTERIZING COHERENT STATES

A. Methodology for implementing and analyzing the DMD

In order to realize the WWT regimes of the GPE, following Ref. [12], using a Fourier based pseudospectral decomposition in space, we run the simulations over a domain of size $L = 128$ with a total of $K_T = 512$ modes in each spatial direction. Using a two stage Runge-Kutta scheme with a time step of $\delta t = 0.1$ for the low-frequency forcing and $\delta t = 0.075$ for the high-frequency forcing, by simulating up to $t_f = 1.5 \times 10^4$, we are able to capture the complex dynamics that we are interested in. These choices for numerical time steps kept the simulations stable and accurate without sacrificing too much computational speed and efficiency as well. Conforming to the

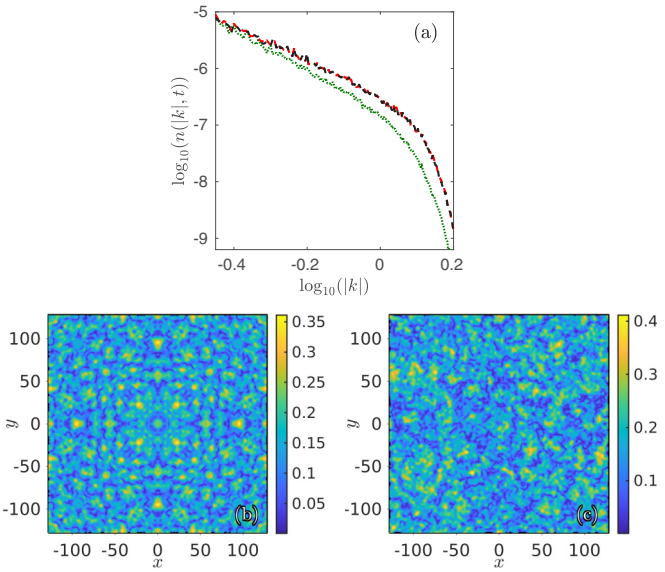

FIG. 1. Low-frequency forcing case with $k_l = 4$, $k_h = 6$, and $\gamma_0 = 2.1 \times 10^{-3}$ under the presence of hyperviscosity and hypoviscosity with respective strengths $\nu_h = 2 \times 10^{-6}$ and $\nu_l = 1 \times 10^{-18}$ and power $p = 8$ with $t_f = 1.5 \times 10^4$. Panel (a) depicts the wave-action spectrum distribution $n(k, t)$ [see Eqs. (8) and (7)] for times $t = t_f/2$ (dotted green curve), $t = 0.98t_f$ (dashed red curve), and $t = t_f$ (black solid curve). The curves for $t = 0.98t_f$ and $t = t_f$ are almost indistinguishable from each other, suggesting that the system has reached equilibrium. Panels (b) and (c) depict the field's amplitude $|\psi(x, y, t)|$ for, respectively, $t = t_f/2$ and $t = 0.98t_f$.

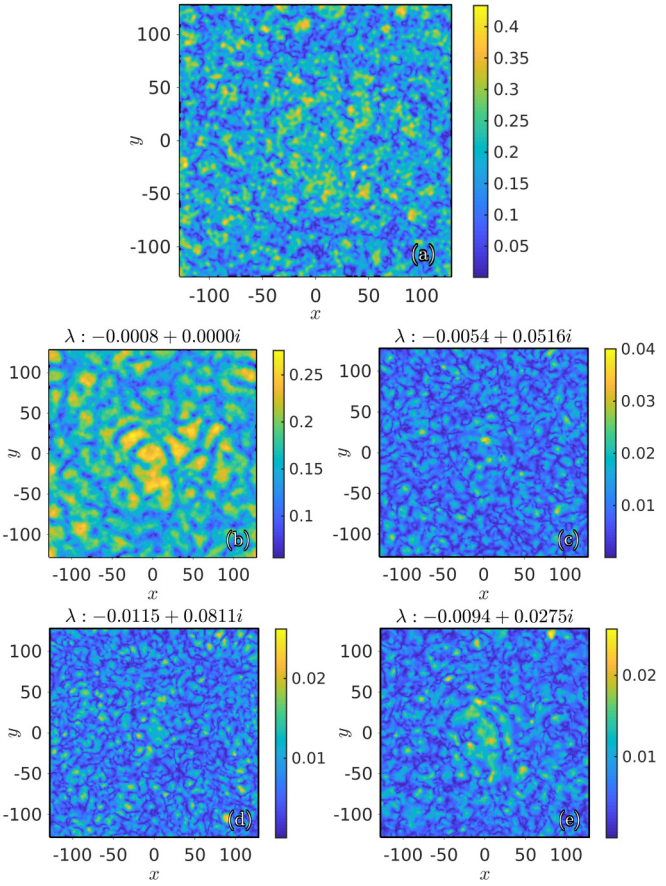

FIG. 2. DMD decomposition for the weak wave turbulence case. This case corresponds to a low-frequency forcing with $k_l = 4$, $k_h = 6$, and $\gamma_0 = 2.1 \times 10^{-3}$ under the presence of hyperviscosity and hypoviscosity with respective strengths $\nu_h = 2 \times 10^{-6}$ and $\nu_l = 1 \times 10^{-18}$ and power $p = 8$. Depicted are (a) the amplitude $|\psi(x, y, t_f)|$, (b) the $\lambda = 0$ DMD mean mode, and (c)–(e) the next three most significant weakly transient modes, i.e., $b_{f(j;n)}\phi_{f(j;n)}$ for $j = 2, 3, 4$. The corresponding eigenvalue for each mode is indicated. In contrast with the next two figures, we do not depict the phase of the wave function here as it does not contain any prominent features because, for this low-frequency forcing case, no vortex structures are nucleated.

choices in Ref. [12], we typically choose $\nu_h = 2 \times 10^{-6}$, $\nu_l = 1 \times 10^{-18}$, and $p = 8$. These choices also reflect the minimal values necessary to generate reliable long time dynamics that produce complex or turbulent dynamics on reasonable simulation time scales.

Throughout each simulation, we sample every five numerical time steps in the low-frequency forcing cases and every seven numerical time steps in the high-frequency case, so that the sampling rate is $\delta t_s = 0.5$ and $\delta t_s = 0.525$, respectively. Different choices of sampling rates were explored with these choices appearing to give the most robust and readily understandable results.

We begin sampling at time t_i corresponding to the last two percent of the total time steps, so that we sample the last 300 units of time, thereby ensuring we are in fact performing DMD on a fully turbulent or mixed flow. To justify this decision, letting $t_f = 1.5 \times 10^4$, in panels (b) and (c) of Fig. 1 we compare the plot of $|\psi(x, y, t)|$ at $t = t_f/2$ to that of $|\psi(x, y, t)|$ at $t = 0.98t_f$; see Fig. 2(a) for the plot of $|\psi(x, y, t)|$ at $t = t_f$. Likewise, in Fig. 1(a) we compare $n(k, t)$, from Eq. (8), at times $t = t_f/2$, $0.98t_f$, and $t = t_f$. As can be seen, while relatively small-scale features have emerged in the flow by $t = t_f/2$, the underlying spatial symmetry of the forcing is still plainly present. This symmetry has clearly been removed at $t = 0.98t_f$. Furthermore, we see that the spectra $n(k, t)$ are essentially identical for $t = 0.98t_f$ and t_f, while there is markedly less energy in the higher-frequency components at $t = t_f/2$. Based on these results we are confident that the last two percent of the flows examined throughout the remainder of the paper represent "equilibrated turbulent" flows, at least in the same sense that is meant in Ref. [12].

Proceeding, we have the approximation

$$g_n \approx A\left(t_n^{(s)}\right) = \sum_{j=1}^{N} b_j e^{\lambda_j (t_n^{(s)} - t_i)} \phi_j, \tag{17}$$

where

$$\lambda_j = \frac{\log \mu_j}{\delta t_s}, \quad t_n^{(s)} = t_i + n\delta t_s, \quad n \geqslant 0. \tag{18}$$

As we see in the simulations, typically each generated DMD mode has a corresponding temporal eigenvalue λ_j such that $-0.02 \leqslant \mathrm{Re}(\lambda_j) \leqslant 0$, suggesting that all modes (with some rare exceptions, see below) are either stationary or transitory. This is in accord with the fact that we are looking at a

driven Hamiltonian system in which we are mainly examining dynamics within the inertial range, so that the dynamics is largely represented via a measure preserving flow, thereby insuring nearly imaginary spectra of the associated Koopman operator. See Appendix B for more details.

To perform mode selection, we implement the following strategy. At each discrete sampling time $t_n^{(s)}$, we sort the sequence

$$\left\{\left|b_j e^{\lambda_j (t_n^{(s)} - t_i)}\right|\right\}_{j=1}^{N} \tag{19}$$

according to magnitude from largest to smallest, inducing a mapping between indices, say $j = f(l;n)$. It is important to note, by emphasizing the sampling step n, we are drawing attention to the fact that the sorting map between indices *can change* at every discrete sampling step. We then select from this sorted list the minimal number of modes, say $N_r(n)$, such that

$$\frac{\left|\left|A_{N_r(n)}\left(t_n^{(s)}\right) - \left|\psi\left(\cdot,\cdot,t_n^{(s)}\right)\right|\right|_2}{\left|\left|\psi\left(\cdot,\cdot,t_n^{(s)}\right)\right|\right|_2} \leqslant 0.1, \tag{20}$$

where

$$A_{N_r(n)}\left(t_n^{(s)}\right) = \sum_{l=1}^{N_r(n)} b_{f(l;n)} e^{\lambda_{f(l;n)}(t_n^{(s)} - t_i)} \phi_{f(l;n)}. \tag{21}$$

Thus $N_r(n)$ represents the minimal number of maximally sorted modes which represent 90% of the total energy of the GPE at $t_n^{(s)}$. Similarly, we define the time dependent compression ratio $C_r(n) = N_r(n)/N$ measuring the proportion of modes needed to describe the bulk of the dynamics (i.e., 90% of the energy). We note that throughout each simulation presented in what follows, if we use all of the available modes, the relative error measured above is at most on the order of 10^{-11} over the course of the DMD sampling process, or the norms of the residuals $\mathbf{r}_n$ are only at worst $10^{-11}||\psi(\cdot,\cdot,t_n^{(s)})||_2$. In other words, taken in its entirety, the DMD provides an extremely accurate reconstruction of the flow over the time which it is applied.

While in some sense an arbitrary choice, we have found the 90% threshold to provide an efficient way to determine the most relevant modes while still providing significant reductions in the compression ratio, thus reflecting the way in which the DMD method is able to capture many of the features of complex flows via relatively low-dimensional representations. As noted above, the modes of interest can change from sampling step to sampling step. To quantify the effect of this change, we measure the Jaccard index [30]

$$\mathcal{J}(n) = \frac{|I_n \cap I_{n-1}|}{|I_n| + |I_{n-1}| - |I_n \cap I_{n-1}|},$$

$$I_j = \{f(1;j), f(2;j), \ldots, f(N_r(j);j)\}, \tag{22}$$

with $|\cdot|$ denoting the number of elements in a given set of indices. As suggested from our results below, in practice it is clear that the DMD method converges onto a stable subset of modes over longer time scales. However, our mode selection scheme also allows us to better understand the dominant processes happening over the length of time of the DMD sampling, thereby allowing for observations of transitory and multiple-scales behavior.

Focusing then on those modes which will ultimately dominate towards the end of the DMD process, given that the total time scale over which we perform the DMD is 300 units of nondimensional time, we define those modes such that $-0.02 \leqslant \mathrm{Re}(\lambda_j) \leqslant 5 \times 10^{-3}$ to be weakly transitory. This choice reflects results from the simulations where it is typical to see the magnitude of the coefficients b_j to be on the order of 10^2 for $\mathrm{Re}(\lambda_j) \sim -0.02$ and 10^{-2} for $\mathrm{Re}(\lambda_j) \sim 0.005$. Our definition of a weakly transitory mode ensures then that an initial amplitude of 10^2 is scaled to 0.5, or just a little over ten percent by the end of the DMD sampling process. Likewise, an initial amplitude of 10^{-2} becomes at most 0.02. Thus, by focusing on these weakly transitory modes, we can focus on those modes which characterize our 90% energy criterion over longer time scales.

B. Modal descriptions

We first examine the results of the DMD by probing the most significant modes which represent the amplitude of the flow at the final time $t_f = 1.5 \times 10^4$.

1. Weak-wave turbulence case

In this case, we take a low frequency band for the forcing with $k_l = 4$, $k_h = 6$ and strength $\gamma_0 = 2.1 \times 10^{-3}$. To recreate the WWT results of Ref. [12], we keep both hypoviscosity and hyperviscosity in place; see Fig. 2. In particular, we see in panel (a) the fully evolved amplitude of the GPE at t_f, i.e., $|\psi(x,y,t_f)|$, compared against the DMD computed mean, i.e., $\lambda = 0$ mode, depicted in panel (b). As seen, we can characterize the WWT regime in part by noting the lack of clear structure in the mean mode. Note, however, that there is a weak circular symmetry present in the mean mode due to the spatially symmetric forcing being centered at the origin. The finer details seen in panel (a) can in part be recovered by looking beyond the mean mode to higher oscillatory or weakly transitory modes as depicted in panels (c)–(e). It is relevant to mention that, by a plot of a weighted DMD mode, we mean that we plot $|b_j U\tilde{\phi}_j|$, thereby allowing us to visualize the spatial structure associated with the mode as well as its relative contribution controlled by the magnitude of b_j, since each mode $U\tilde{\phi}_j$ is scaled to have unit vector norm.

2. Low-frequency saturation case

Through the remaining simulations, we remove the hypoviscosity ($\nu_l = 0$) while keeping the hyperviscosity ($\nu_h = 2 \times 10^{-6}$) with $\gamma_0 = 2.1 \times 10^{-3}$, thereby allowing for saturation at longer wavelengths to occur. In this case, we expect the formation of long-wavelength coherent structures characterized by the presence of relatively few vortices on an elevated density background with acoustic waves scattering throughout. This is indicative of the "Kibble-Zurek" mechanism discussed in Refs. [12,31] used to explain analogies between coherent structure formation in BECs and cosmology. After removing the hypoviscosity, by looking at the relatively low frequency forcing explored above, it is at this point that we can plainly see the advantage of using the DMD by comparing the fully

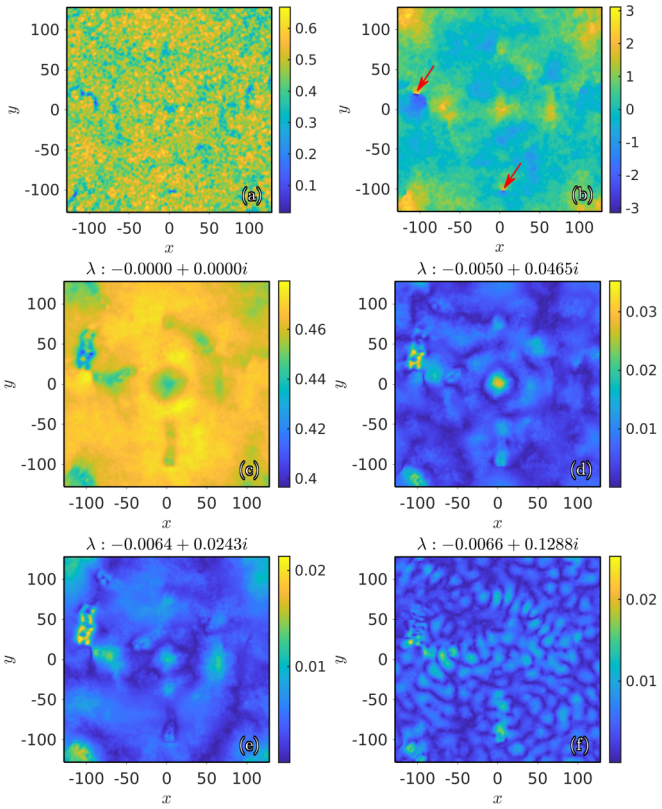

FIG. 3. DMD decomposition for the low-frequency saturation case. Same parameter values as in Fig. 2 after removing the hypoviscosity ($\nu_l = 0$). Depicted are (a) the amplitude $|\psi(x, y, t_f)|$, (b) the phase of the wave function (assumed not to be observable in our methodology), (c) the $\lambda = 0$ DMD mean mode, and (d)–(f) the next three most significant weakly transient modes, i.e., $b_{f(j;n)}\phi_{f(j;n)}$ for $j = 2, 3, 4$. The corresponding eigenvalue for each mode is indicated. In the phase plot we indicate with (red) arrows the location of two vortex-dipole pairs.

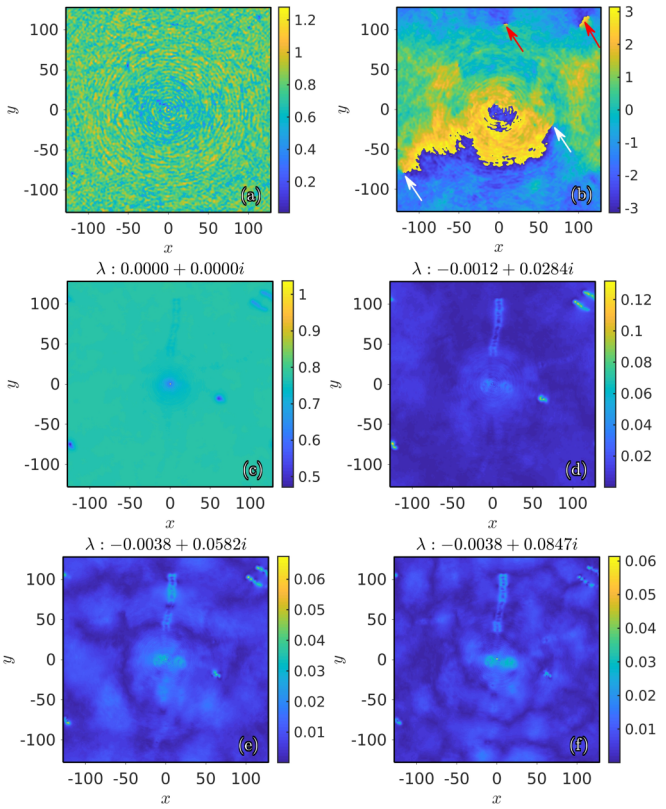

FIG. 4. DMD decomposition for the high-frequency case. Same parameters and layout as in Fig. 3 but this time for a high-frequency forcing with $k_l = 60$ and $k_h = 63$. In the phase plot we indicate with red and white arrows the respective locations of two vortex-dipole pairs and two independent vortices.

evolved solution to the GPE in Fig. 3(a) to the mean DMD mode depicted in Fig. 3(c). The mean mode clearly identifies a finite number of vortices interacting through a finite amplitude background. We can establish that these dips in $|\psi|$ are in fact vortices by examining the phase of ψ, which we have from our numerics. The dips we see in Fig. 3(c) correspond to windings in the phase plotted in Fig. 3(b). Specifically, the phase plot indicates the presence of two vortex-dipole pairs (location indicated with the arrows in the panel). It is interesting to note that these two vortex-dipole pairs are visible in the DMD modes despite the fact that no phase information was used to obtain these modes. It is also evident that tight vortex dipoles move relatively fast in the flow and thus are "smeared out" by the DMD decomposition. Therefore, as can be noticed in Fig. 3 the vortex dipole with the largest separation (top left) is more visible in the DMD modes than the vortex dipole with the tighter separation (bottom center).

It is crucial to stress that we are able to clearly capture the presence of vortices via the DMD without the assistance of any phase information (as we are only measuring the magnitude of the wave function). If one had direct access to the wave functions' phase, then it would be straightforward to extract the location (and sign) of vortices by computing the vorticity of the fluid velocity associated with the BEC flow (see, for instance, Ref. [32] and references therein). However, most experiments lack the possibility of directly measuring the phase of the wave function [33], in which case the DMD proposed here could serve as a valuable tool to extract the location of any vortex present in the condensate—albeit the fact that the DMD cannot directly indicate the sign of said vortices. One of the main advantages of the DMD method in detecting vortices (or other long-lived coherent structures) hinges on the fact that they are clearly visible in the lowest DMD modes (see Figs. 3 and 4). Thus these distinctive structures in the DMD modes cannot be confounded with *transient* density dips that could provide false positives for the presence of a vortex.

It is interesting to note the relative similarity in the finer, higher-frequency features seen in Figs. 3(d)–3(f) to those in Figs. 2(c)–2(e). This suggests that it is possible to characterize the low-frequency saturation case as a long-wave condensed mean containing CSs with a weakly turbulent background fluctuating about this mean.

3. *High-frequency saturation case*

We now look at higher-frequency forcing where we let $k_l = 60$ and $k_h = 63$; see Fig. 4. As in the low-frequency, long-wavelength saturated case above, we see that the

mean DMD mode depicted in panel (c) clearly isolates the dynamics of the vortices present in the configuration, which are obscured through the higher-frequency spatial features in the solution to the GPE depicted in panel (a). This again is confirmed by looking at the phase in Fig. 4(b). Specifically, the phase profile indicates the presence of two independent vortices (see white arrows) and two vortex-dipole pairs (see red arrows). As the independent vortices drift slowly through the flow, they have a high contrast in the DMD modes. On the other hand, as before, tight (i.e., fast moving) vortex-dipole pairs have a relatively weaker contrast in the DMD modes. However, in contrast with the low-frequency forcing case above though, we see in the higher-order modes in panels (d)–(f) far sharper, or higher-frequency, spatial features, thus clearly reflecting the different forcing mechanism in play in this situation. This is particularly true for the fast moving vortex-dipole pairs which remain clearly visible in the DMD modes for the high-frequency case when compared to the low-frequency one. Finally, it is worth mentioning that the DMD analysis not only provides evidence of the presence of coherent structures such as vortices, but it also gives a sense of their dynamics. For instance, it is clear from the higher-order DMD modes depicted in Fig. 4 what is the trajectory of the vortex-dipole pairs. Namely, the center top pair moves up vertically relatively fast, while the top-right pair moves slowly in a north-west diagonal trajectory. Interestingly, the contrast of the trace left by the coherent structure's trajectory could be used as a measure for their corresponding speed through their trajectory: the fainter the trace, the faster the speed.

C. Comparison across flows via spectral characteristics

We now compare the spectral characteristics and compression ratios for the WWT, the low-frequency saturation (LFS), and high-frequency saturation (HFS) cases studied above. Here, we focus less on isolating some relatively small number of modes and opt to examine the characteristic responses of each measured quantity across the different flows, thereby allowing for the identification of classifying features that may not be as readily apparent given the overall complexity of each flow. As observed in the left panels of Fig. 5, all the modes, with the exception of the ones highlighted using triangular and circular points, have eigenvalues with negative real parts. This indicates that all these modes are weakly damped and thus weakly transitory. Among the modes which are weakly transitory, the mean (see triangular points) always begins as the dominant mode with respect to its magnitude of $|b_j|$. Note that in the WWT regime, see panel (a) in Fig. 5, there is a mode (see circular point) with an eigenvalue with a small, but positive, real part [$\mathrm{Re}(\lambda_i) \approx 5 \times 10^{-3}$]. This mode, although identified as a growing one, has a relatively small magnitude ($b_j \approx 0.009$) and thus very weakly participates in the DMD. In fact, using the 90% energy mode selection criterion, this mode is not even part of the selected basis. On the other hand, we see from the right set of panels in Fig. 5 that the higher temporal frequencies of oscillation correspond to smaller magnitudes of $|b_j|$, reflecting a kind of energy decay in time akin to what one usually sees via Fourier transforms in time or space. However, focusing on the regime of weakly

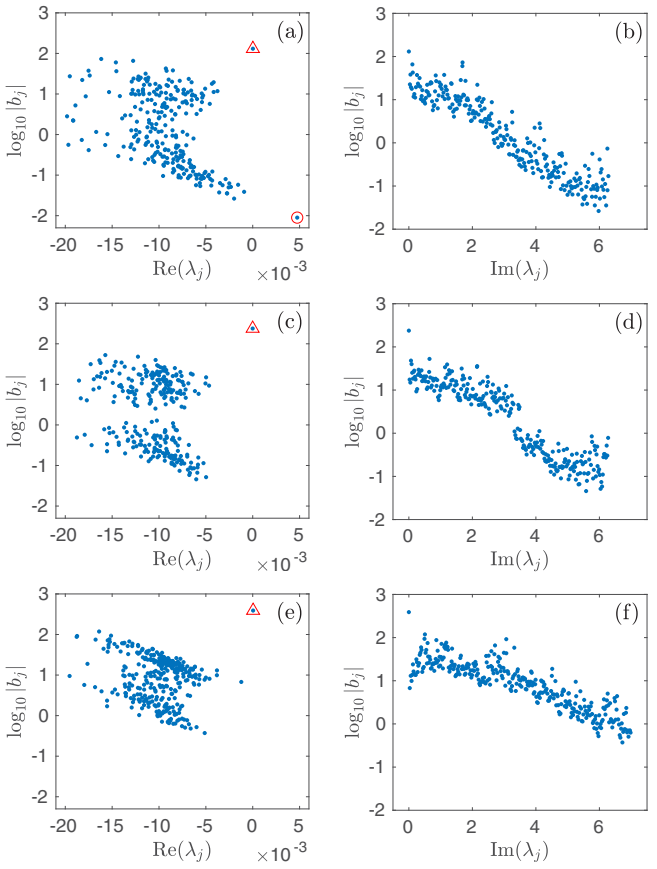

FIG. 5. Spectra of the DMD modes. The left (right) panels depict $\log_{10}|b_j|$ vs the real (imaginary) part of λ_j. The top, middle, and bottom set of panels correspond, respectively, to the WWT, low-frequency saturated, and high-frequency saturated regimes. The triangular points in the left panels correspond to the eigenvalues of the weighted mean. The mode depicted by the circle in panel (a) corresponds to a weakly growing mode with a relatively small weight ($b_j \approx 0.009$) such that it does not have a sizable contribution to the DMD dynamics.

transitory modes, we see marked differences in the spread of the magnitudes of $|b_j|$ with respect to the real part of the eigenvalues λ_j. Thus the way in which weakly transitory effects manifest themselves are distinguished in the different classes of flows.

The impact of the spectra described above manifests itself in the different dynamics and long time behavior of the compression ratio $C_r(n)$ and the Jaccard indices $\mathcal{J}(n)$ as depicted in Fig. 6. As can be observed, the greater complexity of the WWT flow necessitates larger and, at times, more erratic numbers of modes in order to maintain the 90% threshold used for modal selection. This likewise manifests as significant fluctuations in $\mathcal{J}(n)$ before it ultimately settles into a state in which the selected modes overlap by about 95%. We also see the greater complexity in the HFS case in comparison to the LFS case by way of the overall larger compression ratio needed in the HFS case throughout most of the simulation; see in particular the detail plots in panels (g) and (h) of Fig. 6. Moreover, we see that the Jaccard index is more volatile in the HFS case, with strong deviations in the choice of

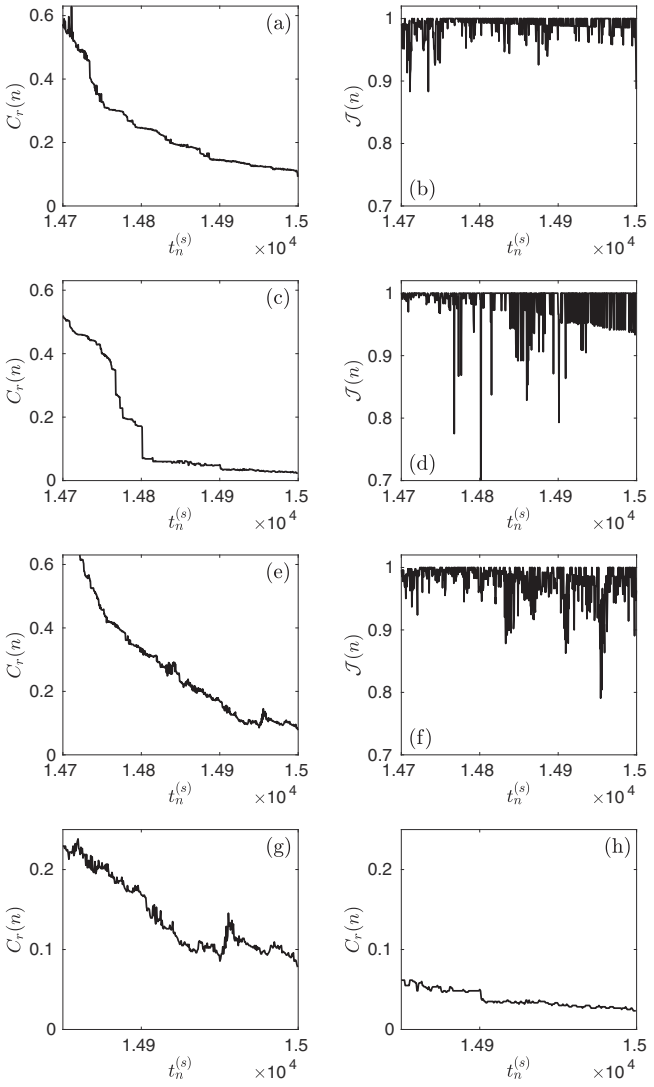

FIG. 6. (a)–(f) Evolution of the compression ratio $C_r(n)$ (left) and Jaccard index $\mathcal{J}(n)$ (right) corresponding, from top to bottom, to the WWT, low-frequency saturated, and high-frequency saturated regimes. Panels (g) and (h) depict details of the compression ratio for the high-frequency and low-frequency saturated regimes, respectively.

finite-dimensional subspace even close to the end of the simulation. We note that the comparison of the Jaccard index in the LFS and HFS cases must be made with the compression ratio in mind. By this we mean that, while there is volatility in $\mathcal{J}(n)$ for both cases, this volatility is over a far larger subspace in the HFS case than in the LFS case as seen by comparing the details of the compression ratio plots in panels (g) and (h). A partial explanation for this is that in the HFS case, in order for energy to transfer to the longer wavelengths, one must first form the higher frequency contributions and spindle CSs structures as seen in Figs. 4(c)–4(e). Lastly, we note the presence of jumps in the compression ratio which clearly correspond, predominantly, to the more transitory modes, determined from examining the most leftward eigenvalues depicted in the left panels of Fig. 6.

V. CONCLUSIONS

In the present work, we simulated different turbulent flows in a 2D BEC modeled by the Gross-Pitaevskii equation with stochastic, band-limited, forcing. The injection of energy through the forcing was balanced by energy removal at both ends of the energy spectrum by adding hypoviscosity and hyperviscosity phenomenological terms in the model equation. We borrowed the dynamic-mode decomposition (DMD) methodology in order to characterize the nature of the obtained complex flows corresponding to weak-wave turbulence, low-frequency saturation, and high-frequency saturation regimes. In view of deploying the DMD methodology to more general complex flows, including ones coming from experimental realizations, we extracted and ranked the DMD modes so to only keep a small, manageable, percentage of them. The modal selection ranking was defined by keeping all modes necessary to reconstruct 90% of the energy of the system. This dynamic reduction resulted in keeping just 10% of the total number of modes. Within this reduced modal set, we used the spectral information of the modes to characterize the different turbulent regimes. This information was used in tandem with (a) the compression ratio that gives a measure of the proportion of modes necessary to capture the desired level of energy with the DMD subset and (b) the Jaccard index of the modal set which provides a measure of the stationarity of the chosen modal set.

Our results tend to suggest that the DMD decomposition is successful in differentiating the distinct types of complex flows and, in particular, it seems to be very useful in extracting coherent structures that might otherwise be hidden in the complexity of the flow. For instance, we were able to extract the location (and some of the dynamics) of vortices despite the fact that we did not use any phase information of the BEC flow to build the DMD modal set. This feature of the DMD to be able to detect hidden coherent structures seems particularly appealing in the realm of atomic BEC where vortices cannot be readily pinpointed without the use of the wave function's phase, which is typically not available in most atomic BEC experiments. For instance, it would be interesting to use the DMD methodology for BEC flows that, by construction, promote the nucleation of coherent structures (such as vortices; cf. Refs. [34,35]) in order to separate the dynamics associated with these coherent structures and the complex background flow.

The DMD methodology is, by construction, model agnostic and it is well suited for experimental situations where a large amount of data is usually extracted. Therefore, it is a good candidate to provide useful information about the main characteristics of complex flows and the potential hidden coherent structures that they might host. It would be interesting to test whether the results presented here are relevant to other complex flow scenarios like classical flows and whether the DMD is useful to indeed characterize and differentiate different turbulent states.

ACKNOWLEDGMENTS

C.W.C. gratefully acknowledges the support of Grant No. NSF-DMS-1715039. R.C.-G. gratefully acknowledges the

support of Grant No. NSF-PHY-1603058. The authors also wish to thank the anonymous reviewers for their careful reading and suggestions, which have greatly improved this paper.

APPENDIX A: DIMENSIONAL REDUCTION AND NONDIMENSIONALIZATION OF THE GPE

In physical units, an unforced 3D BEC, trapped in a harmonic potential $V(x,y,z)=\frac{1}{2}(\omega_x^2x^2+\omega_y^2y^2+\omega_z^2z^2)$, can be modeled, for temperatures close to zero, by the Gross-Pitaevskii equation [26]:

$$i\hbar\frac{\partial}{\partial t}\psi_{3D}=\left[-\frac{\hbar^2}{2m}\Delta+g_{3D}|\psi_{3D}|^2+V(x,y,z)\right]\psi_{3D}, \quad \text{(A1)}$$

where $\psi_{3D}(x,y,z,t)$ is the 3D wave function, ω_i are the trapping frequencies (strengths) of the confining trap along the three cardinal directions, and the nonlinearity $g_{3D}=4\pi\hbar^2a_s/m$ is given in terms of the s-wave scattering length a_s and the mass of the atoms m. In this 3D setting, $|\psi_{3D}|^2dx\,dy\,dz$ describes probabilities in the sense that

$$\mathcal{N}=\iiint|\psi_{3D}|^2dx\,dy\,dz \quad \text{(A2)}$$

recovers the total number of particles under consideration. A 2D reduction of the BEC can then be achieved by assuming that one of the trapping strengths is much larger than the other two, i.e., $\omega_x,\omega_y\ll\omega_z$. In that case, one can separate the full 2D wave function as

$$\psi_{3D}(x,y,z,t)=\psi_{2D}(x,y,t)\times\psi_0(z)\times e^{-i\mu_zt/\hbar}, \quad \text{(A3)}$$

where $\psi_{2D}(x,y,t)$ is the effective 2D wave function and $\psi_0(z)$ is the z-ground state with chemical potential μ_z. The above separation is based on the assumption that, when dealing with moderate energies, the ω_z is large enough so that excitations along the z direction cannot be promoted and thus the wave function always remains in its ground state along this transverse direction. Then, by normalizing $\psi_0(z)$, applying the separation of variables (A3), and averaging (i.e., integrating) along the z direction, one obtains the effective 2D GPE

$$i\hbar\frac{\partial}{\partial t}\psi=\left[-\frac{\hbar^2}{2m}\Delta+g_{2D}|\psi|^2\right]\psi, \quad \text{(A4)}$$

where we have assumed very weak trapping strengths in the x and y directions ($\omega_x,\omega_y\simeq 0$). In this 2D reduction, the new effective 2D nonlinearity is given by

$$g_{2D}=\frac{g_{3D}}{\sqrt{2\pi}a_z} \quad \text{(A5)}$$

and $a_z=\hbar/(m\omega_z)$ is the transverse oscillator length. It is remarkable that, in this setting, one can use the transverse trapping strength ω_z to control the effective nonlinearity of the 2D reduced model. As the transverse wave function $\psi_0(z)$ is normalized, $|\psi(x,y,t)|^2$ now describes the (probability) density in 2D and thus

$$\mathcal{N}=\iint|\psi_{2D}|^2dx\,dy \quad \text{(A6)}$$

now recovers the total number of particles under consideration. Finally, introducing the scalings (oscillator length units)

$$\tilde{x}=\frac{x}{\sqrt{2}\xi}, \quad \tilde{y}=\frac{y}{\sqrt{2}\xi}, \quad \tilde{t}=\omega_zt, \quad \tilde{\psi}=\sqrt{\frac{\hbar\omega_z}{g_{2D}}}\psi, \quad \text{(A7)}$$

where

$$\xi^2=\frac{\hbar}{m\omega_z} \quad \text{(A8)}$$

is the so-called healing length, yields (after dropping the tildes for ease of notation) the nondimensional 2D GPE

$$i\psi_t=-\Delta\psi+\sigma|\psi|^2\psi, \quad \text{(A9)}$$

where $\sigma=\mathrm{sgn}(a_s)$ defines the sign of the nonlinearity corresponding to an attractive, or self-focusing, BEC for $\sigma=-1$ and to a repulsive, or defocusing, BEC for $\sigma=1$.

APPENDIX B: OBSERVABLES FOR THE HAMILTONIAN FLOW

Throughout this section, we ignore the effects of forcing and damping so as to make deriving motivating results relatively straightforward. Thus, starting from the well-known Hamiltonian of the GPE/NLSE

$$H=\int|\nabla\psi|^2d\mathbf{x}+\frac{1}{2}\int|\psi|^4d\mathbf{x}, \quad \text{(B1)}$$

the GPE may be rewritten in variational form as

$$i\psi_t=\frac{\delta H}{\delta\psi^*}. \quad \text{(B2)}$$

Using a Fourier expansion, we get the equivalent Hamiltonian system

$$i\partial_ta_{\mathbf{m}}(t)=\frac{\delta H}{\delta a_{\mathbf{m}}^*(t)}, \quad \text{(B3)}$$

where $H>0$ becomes

$$H=\sum_{\mathbf{m}}\omega(k_{\mathbf{m}})|a_{\mathbf{m}}|^2+\frac{1}{2}\sum_{\mathbf{m}_1,\mathbf{m}_2,\mathbf{m}_3,\mathbf{m}}a_{\mathbf{m}_1}a_{\mathbf{m}_2}a_{\mathbf{m}_3}^*a_{\mathbf{m}}^*\delta_{\mathbf{m}_1,\mathbf{m}_2}^{\mathbf{m},\mathbf{m}_3}, \quad \text{(B4)}$$

where

$$\delta_{\mathbf{m}_1,\mathbf{m}_2}^{\mathbf{m},\mathbf{m}_3}=\delta(\mathbf{m}_1+\mathbf{m}_2-\mathbf{m}_3-\mathbf{m}), \quad \text{(B5)}$$

with $\delta(\cdot)$ being the Kronecker delta function or tensor.

To truncate the system so that it is consistent with the pseudospectral method that we employ to integrate the GPE, we introduce the wraparound function τ where, letting $K_T=2K+1$, if we define for an integer $\tilde{m}$ the function

$$\tau(\tilde{m})\in\{-K,\ldots,0,\ldots,K\}, \quad \text{(B6)}$$

so that

$$(\tilde{m}+K)\equiv(\tau(\tilde{m})+K)\mathrm{mod}\,K_T, \quad \text{(B7)}$$

then if $\mathbf{m}=(m,n)$, we define $\tau(\mathbf{m})$ so that

$$\tau(\mathbf{m})=(\tau(m),\tau(n)). \quad \text{(B8)}$$

This allows us to account for the effect of aliasing due to nonlinearity in our pseudospectral method. We then require that

$$0 \leqslant ||\mathbf{m}||_\infty \leqslant K, \quad ||\mathbf{m}||_\infty = \max\{|m|, |n|\}, \tag{B9}$$

which yields the affiliated dynamical system

$$i\partial_t a_{\mathbf{m}} = F_{\mathbf{m}}(\mathbf{a}), \quad \mathbf{a} \in \mathbb{C}^{2K+1}, \quad 0 \leqslant ||\mathbf{m}||_\infty \leqslant K, \tag{B10}$$

where $\mathbf{a} \in \mathbb{C}^{(2K+1)^2}$ denotes the set of all the $a_{\mathbf{m}}$ values and where

$$F_{\mathbf{m}}(\mathbf{a}) = \omega(k_{\mathbf{m}})a_{\mathbf{m}} + \sum a_{\mathbf{m}_1} a_{\mathbf{m}_2} a^*_{\tau(\mathbf{m}_1+\mathbf{m}_2-\mathbf{m})}, \tag{B11}$$

where the sum is carried out for $0 \leqslant ||\mathbf{m}_1||_\infty, ||\mathbf{m}_2||_\infty \leqslant K$. We define the affiliated flow for initial conditions $\mathbf{a}_0$ via the flow map $\Phi(t; \mathbf{a}_0)$. We readily see that the functional

$$\tilde{H}(\mathbf{a}; K) = \sum_{0 \leqslant ||\mathbf{m}||_\infty \leqslant K} \omega(k_{\mathbf{m}})|a_{\mathbf{m}}|^2 + \frac{1}{2}\sum a_{\mathbf{m}_1} a_{\mathbf{m}_2} a^*_{\tau(\mathbf{m}_3)} a^*_{\tau(\mathbf{m})} \delta^{\mathbf{m},\mathbf{m}_3}_{\mathbf{m}_1,\mathbf{m}_2}, \tag{B12}$$

where the second sum is carried out for $0 \leqslant ||\mathbf{m}||_\infty, ||\mathbf{m}_1||_\infty, ||\mathbf{m}_2||_\infty, ||\mathbf{m}_3||_\infty \leqslant K$, provides a Hamiltonian of the finite-dimensional system.

Fixing the number of modes, K, one can define the density

$$\rho(\mathbf{a}) = \frac{1}{Z} e^{-\tilde{H}(\mathbf{a};K)}, \tag{B13}$$

where the normalization constant is $Z = \int_{\mathbb{C}^{(2K+1)^2}} e^{-\tilde{H}(\mathbf{a};K)} d\mathbf{a}$. Following Ref. [28], this yields the average, or expectation, functional $\mathrm{E}[f]$ for any well-defined observable f to be

$$\mathrm{E}[f] = \int_{\mathbb{C}^{(2K+1)^2}} f(\mathbf{a})\rho(\mathbf{a}) d\mathbf{a}. \tag{B14}$$

From the density, we can define an invariant measure μ, which allows us to readily define the affiliated Hilbert space $L_2(\mathbb{C}^{(2K+1)^2}, \mu)$ with inner product $\langle f, g\rangle = \mathrm{E}[fg]$. Using the method of characteristics, we can define for our flow the associated Liouville operator $\mathcal{L}$ so that the solution to the equation

$$u_t = \mathcal{L}u, \quad u(\mathbf{a}_0, 0) = g(\mathbf{a}_0) \in L_2(\mathbb{C}^{(2K+1)^2}, \mu) \tag{B15}$$

has the solution

$$u(\mathbf{a}_0, t) = e^{\mathcal{L}t} g(\mathbf{a}_0) = g(\Phi(t, \mathbf{a}_0)). \tag{B16}$$

Using the semigroup property of $e^{\mathcal{L}t}$ and Φ, we see that, by choosing a fixed time step δt, we have

$$g(\Phi(t + \delta t, \mathbf{a}_0)) = e^{\mathcal{L}\delta t} g(\Phi(t, \mathbf{a}_0)). \tag{B17}$$

Thus, for any reasonably defined quantity g, there exists a linear operator $e^{\mathcal{L}\delta t}$ which transports that quantity forward in discrete steps of time. The Hamiltonian structure of the underlying finite-dimensional system ensures that $e^{\mathcal{L}\delta t}$ is a unitary operator, which is to say that it preserves the $L_2(\mathbb{C}^{(2K+1)^2}, \mu)$ norm of a given function. Thus the linear Koopman operator is given in our Hamiltonian context by $e^{\mathcal{L}\delta t}$. Generalizations of this approach are found in Refs. [20,22,23] and elsewhere.

[1] J. A. Seman, E. A. L. Henn, R. F. Shiozaki, G. Roati, F. J. Poveda-Cuevas, K. M. F. Magalhães, V. I. Yukalov, M. Tsubota, M. Kobayashi, K. Kasamatsu, and V. S. Bagnato, Route to turbulence in a trapped Bose-Einstein condensate, Laser Phys. Lett. **8**, 691 (2011).

[2] T. W. Neely, A. S. Bradley, E. C. Samson, S. J. Rooney, E. M. Wright, K. J. H. Law, R. Carretero-González, P. G. Kevrekidis, M. J. Davis, and B. P. Anderson, Characteristics of Two-Dimensional Quantum Turbulence in a Compressible Superfluid, Phys. Rev. Lett. **111**, 235301 (2013).

[3] W. J. Kwon, G. Moon, J.-y. Choi, S. W. Seo, and Y.-i. Shin, Relaxation of superfluid turbulence in highly oblate Bose-Einstein condensates, Phys. Rev. A **90**, 063627 (2014).

[4] P. M. Walmsley and A. I. Golov, Coexistence of Quantum and Classical Flows in Quantum Turbulence in the $t = 0$ Limit, Phys. Rev. Lett. **118**, 134501 (2017).

[5] S. Kang, S. W. Seo, J. H. Kim, and Y. Shin, Emergence and scaling of spin turbulence in quenched antiferromagnetic spinor Bose-Einstein condensates, Phys. Rev. A **95**, 053638 (2017).

[6] E. Varga and L. Skrbek, Dynamics of the density of quantized vortex lines in counterflow turbulence: Experimental investigation, Phys. Rev. B **97**, 064507 (2018).

[7] N. Navon, A. L. Gaunt, R. P. Smith, and Z. Hadzibabic, Emergence of a turbulence cascade in a quantum gas, Nature (London) **539**, 72 (2016).

[8] V. E. Zakharov, Weak turbulence in media with decay dispersion law, Zh. Prikl. Mekh I Tekhn. Fiz. **4**, 35 (1965) [J. Appl. Mech. Tech. Phys. **6**, 22 (1965)].

[9] S. Nazarenko, *Wave Turbulence* (Springer, New York, 2011).

[10] A. C. Newell, S. Nazarenko, and L. Biven, Wave turbulence and intermittency, Physica D **152–153**, 520 (2001).

[11] D. Cai, A. J. Majda, D. W. McLaughlin, and E. G. Tabak, Dispersive wave turbulence in one dimension, Physica D **152–153**, 551 (2001).

[12] S. Nazarenko and M. Onorato, Wave turbulence and vortices in Bose-Einstein condensation, Physica D **219**, 1 (2006).

[13] N. Mordant and B. Miquel, Intermittency and emergence of coherent structures in wave turbulence of a vibrating plate, Phys. Rev. E **96**, 042204 (2017).

[14] A. C. White, B. P. Anderson, and V. S. Bagnato, Vortices and turbulence in trapped atomic condensates, Proc. Natl. Acad. Sci. USA **111**, 4719 (2014).

[15] T. P. Billam, M. T. Reeves, B. P. Anderson, and A. S. Bradley, Onsager-Kraichnan Condensation in Decaying Two-Dimensional Quantum Turbulence, Phys. Rev. Lett. **112**, 145301 (2014).

[16] P. G. Kevrekidis, D. J. Frantzeskakis, and R. Carretero-González, *Emergent Nonlinear Phenomena in Bose-Einstein Condensates: Theory and Experiment*, Springer Series on Atomic, Optical, and Plasma Physics Vol. 45 (Springer, New York, 2008).

[17] R. Navarro, R. Carretero-González, P. J. Torres, P. G. Kevrekidis, D. J. Frantzeskakis, M. W. Ray, E. Altuntaş, and D. S. Hall, Dynamics of a Few Corotating Vortices in Bose-Einstein Condensates, Phys. Rev. Lett. **110**, 225301 (2013).

[18] T. W. Neely, E. C. Samson, A. S. Bradley, M. J. Davis, and B. P. Anderson, Observation of Vortex Dipoles in an Oblate Bose-Einstein Condensate, Phys. Rev. Lett. **104**, 160401 (2010).

[19] D. V. Freilich, D. M. Bianchi, A. M. Kaufman, T. K. Langin, and D. S. Hall, Real-time dynamics of single vortex lines and vortex dipoles in a Bose-Einstein condensate, Science **329**, 1182 (2010).

[20] I. Mezić, Spectral properties of dynamical systems, model reduction, and decompositions, Nonlinear Dyn. **41**, 309 (2005).

[21] P. Schmid, Dynamic mode decomposition of numerical and experimental data, J. Fluid Mech. **656**, 5 (2010).

[22] M. O. Williams, I. G. Kevrekidis, and C. W. Rowley, A data-driven approximation of the Koopman operator: Extending dynamic mode decomposition, J. Nonlinear Sci. **25**, 1307 (2015).

[23] J. N. Kutz, S. L. Brunton, B. W. Brunton, and J. L. Proctor, *Dynamic Mode Decomposition: Data-driven modeling of complex systems* (SIAM, Philadelphia, PA, 2016).

[24] C. J. Pethick and H. Smith, *Bose-Einstein Condensation in Dilute Gases* (Cambridge University Press, Cambridge, UK, 2011).

[25] L. Erdős, B. Schlein, and H.-T. Yau, Rigorous Derivation of the Gross-Pitaevskii Equation, Phys. Rev. Lett. **98**, 040404 (2007).

[26] P. G. Kevrekidis, D. J. Frantzeskakis, and R. Carretero-González, *The Defocusing Nonlinear Schrödinger Equation* (SIAM, Philadelphia, 2015).

[27] B. O. Koopman, Hamiltonian systems and transformation in Hilbert space, Proc. Natl. Acad. Sci. USA **17**, 315 (1931).

[28] A. J. Chorin, O. H. Hald, and R. Kupferman, Optimal prediction with memory, Physica D **166**, 239 (2002).

[29] M. Korda and I. Mezić, On convergence of extended dynamic mode decomposition to the Koopman operator, J. Nonlinear Sci. **28**, 687 (2018).

[30] P. N. Tan, M. Steinbach, and V. Kumar, *Introduction to Data Mining* (Pearson, New York, 2018).

[31] N. G. Berloff and C. Yin, Turbulence and coherent structures in two-component Bose condensates, J. Low Temp. Phys. **145**, 187 (2006).

[32] A. S. Bradley and B. P. Anderson, Energy Spectra of Vortex Distributions in Two-Dimensional Quantum Turbulence, Phys. Rev. X **2**, 041001 (2012).

[33] A notable exception to the lack of access of the wave function's phase are experiments with polariton condensates where *both* density and phase can be directly extracted with high spatial and temporal resolution (see, for instance, Ref. [36] and references therein).

[34] G. Gauthier, M. T. Reeves, X. Yu, A. S. Bradley, M. Baker, T. A. Bell, H. Rubinsztein-Dunlop, M. J. Davis, and T. W. Neely, Negative-temperature Onsager vortex clusters in a quantum fluid, arXiv:1801.06951.

[35] F. Pinsker and N. G. Berloff, Transitions and excitations in a superfluid stream passing small impurities, Phys. Rev. A **89**, 053605 (2014).

[36] L. Dominici, R. Carretero-González, A. Gianfrate, J. Cuevas-Maraver, A. S. Rodrigues, D. J. Frantzeskakis, G. Lerario, D. Ballarini, M. De Giorgi, G. Gigli, P. G. Kevrekidis, and D. Sanvitto, Interactions and scattering of quantum vortices in a polariton fluid, Nat. Commun. **9**, 1467 (2018).